

Impact of counter anions on structural and magnetic properties of iron(III) *meso*-tetraphenylporphyrin tetrahydrofuran solvates

Tilen Knaflič^{a,b,1}, Mateja Žnidarič^{c,1}, Franc Perdih^{d,1}, Marko Trampuž^c, Zvonko Jagličić^{e,f}, Zdenko Časar^{c,g,*}, Denis Arčon^{a,h,**}

^a Jožef Stefan Institute, Condensed Matter Physics Department, Jamova cesta 39, 1000 Ljubljana, Slovenia

^b Institute for the Protection of Cultural Heritage of Slovenia, Research Institute, Poljanska cesta 40, 1000 Ljubljana, Slovenia

^c Lek Pharmaceuticals d.d., Sandoz Development Centre Slovenia, Kolodvorska 27, 1234 Mengeš, Slovenia

^d University of Ljubljana, Faculty of Chemistry and Chemical Technology, Večna pot 113, 1000 Ljubljana, Slovenia

^e Institute of Mathematics, Physics and Mechanics, Jadranska 19, 1000 Ljubljana, Slovenia

^f University of Ljubljana, Faculty of Civil and Geodetic Engineering, Jamova 2, 1000 Ljubljana, Slovenia

^g University of Ljubljana, Faculty of Pharmacy, Aškerčeva 7, 1000 Ljubljana, Slovenia

^h University of Ljubljana, Faculty of Mathematics and Physics, Jadranska 19, 1000 Ljubljana, Slovenia

ARTICLE INFO

Keywords:

Magnetic materials

X-ray diffraction

Electron paramagnetic resonance (EPR)

Magnetic properties

ABSTRACT

Intensively researched iron *meso*-tetraphenylporphyrin (FeTPP) complexes are central to the functionalities of many biological systems while at the same time they possess intriguing magnetic properties. Here we report on the synthesis and structural characterization of FeTPP complexes with axial tetrahydrofuran (THF) ligand and different non-coordinating counter anions. Structurally, the most interesting feature of these complexes is the stretching of the distance between the iron(III) and the oxygen atom of the THF ligand for different counter anions. This parameter affects the magnetic anisotropy of FeTPP as studied here with magnetic susceptibility, χ_m , and X-band electron paramagnetic resonance (EPR). Both magnetic probes are consistent with the iron(III) in its high-field state $S = 5/2$. Simulations of temperature dependencies of χ_m and EPR spectra show that the zero-field splitting magnetic anisotropy parameter D decreases with the tetragonal elongation of the hexacoordinated iron(III) geometry, which is qualitatively discussed within the ligand field theory.

1. Introduction

Porphyrin-based metal(III) complexes are a well-known group of chemical compounds whose functionalities in many biological systems and magnetic properties can be effectively tuned via the coordination of different transition metals or via the peripheral substitutions [1,2]. Various metals have been utilized in these compounds as paramagnetic centers, including Mn, Fe, etc. and a wide range of porphyrin ligands with different covalent substituents, counter ions, and axial ligands have been reported [3]. These complexes were extensively studied, for example, as molecular magnets offering a versatile platform for the bottom-up design of low-dimensional magnetic materials [4–6]. The performance of such molecular magnets critically depends on the resulting magnetic anisotropies and our ability to tailor them.

While a plethora of studies have been conducted on individual compounds, the number of comparative studies, which deem to understand the correlation between structure and magnetic properties, is considerably lower. Some literature reports have compared different metal ions as paramagnetic centers with the same porphyrin-based ligands [7,8], while other studies focused more on the impact of different substituents on the porphyrin ring with the same metal center present [9,10]. Axial ligands in particular have a strong effect on magnetic properties of metalloporphyrins. Zero-field splitting (ZFS) [11] and derived values of the spin-Hamiltonian parameters were determined for several iron(III) and manganese(III) porphyrins with various halogen and azide ligands [12]. A thorough analysis of a series of *meso*-tetraphenylporphyrinatoiron(III) complexes of general formula FeTPP(Y) where Y is a weak ligand (ClO_4^- , BF_4^- , PF_6^- , SbF_6^- , and CF_3SO_3^-), showed that manipulation of the axial ligand field of a ferric

* Corresponding author. Lek Pharmaceuticals d.d., Sandoz Development Centre Slovenia, Kolodvorska 27, 1234 Mengeš, Slovenia

** Corresponding author. Jožef Stefan Institute, Condensed Matter Physics Department, Jamova Cesta 39, 1000 Ljubljana, Slovenia.

E-mail addresses: zdenko.casar@sandoz.com, zdenko.casar@ffa.uni-lj.si (Z. Časar), denis.arcon@ijs.si (D. Arčon).

¹ These authors contributed equally.

porphyrin leads to spin states which change in a rational manner [13]. A so-called magnetochemical series was later proposed to rank the ligand field strength of these weakly binding anions as axial ligands of iron(III) tetraphenylporphyrine [14]. Magnetization and magnetic anisotropy data were studied in the high-spin complexes [FeTPP(X)] ($X = \text{SCN}^-$, Cl^- , Br^- , and I^-) [15] and later a study with inelastic neutron scattering and *ab initio* calculations of a similar group of [FeTPP(X)] complexes ($X = \text{F}^-$, Cl^- , Br^- , I^-) showed a correlation between the axial anisotropy parameter D and the nature of halide ion [16]. In an extension of this study, high-frequency-high-field electron paramagnetic resonance (HF-EPR) and far-IR magnetic spectroscopy (FIRMS) were utilized on the same series of compounds to determine parameter D more precisely [17]. [MnTPP(X)] halides have also been studied in a similar manner and it was discovered that bromide complex ($X = \text{Br}$) possesses easy-axis anisotropy, while for the iodide analogue D changes sign leading to the easy-plane anisotropy [18]. The dramatic change of sign for D has been ascribed to the presence of ligand-to-metal charge transfer. Therefore, the effect of axial ligands on the ZFS is quite profound and proceeds either through the tuning of metal-halide ligand field or in certain cases even via the charge transfer processes. On the other hand, the non-coordinating counter ion impact on the magnetic properties of metal porphyrins is expected to be more subtle. Literature reports demonstrate that magnetic properties are indeed affected by the different counter anion in iron complexes with tetrazole-based nitrogen ligands [19], but their impact on the properties of metalloporphyrins is yet to be systematically explored.

Several iron(III) TPP complexes with axial THF ligands were previously reported in the literature to form complexes with *N*-nitrosamines [20–23]. Recently, we have studied the interaction between metalloporphyrins and *N*-nitrosamines and synthesized a plethora of different metalloporphyrins for evaluation as potential *N*-nitrosamine chemosensors [24]. In particular, to explore the structure-activity relationship of metalloporphyrins for detection of *N*-nitrosamines, a series of [FeTPP(THF)_{*x*}] complexes with various counter anions were prepared. As these systems comprise tetragonally elongated high-spin d^5 states, the axial ligands may directly influence the precise ZFS values through the spin-orbit coupling contribution [17]. However, this family of complexes allows us also to investigate the effect of counter anions on the magnetic anisotropies. Hence, here we report on the study of the correlation between structural and magnetic (particularly ZFS) properties of selected FeTPP THF-coordinated THF solvates with four different counter ions, specifically in [FeTPP(THF)_{*x*}] $X \cdot x$ THF, where $X = \text{ClO}_4^-$, BF_4^- , SbF_6^- , PF_6^- and x is the number of solvated or coordinated THF molecules, and in axially ligated chloride [FeTPP(THF)Cl] · THF. We discover that variations of non-coordinating counter anions X still affect the parameters of ZFS anisotropy through fine-tuning of iron(III) – axial THF ligand interaction. Therefore, non-coordinating counter anions X provide a parallel way for tailoring magnetic properties of [FeTPP(THF)_{*x*}] $X \cdot x$ THF molecular magnets.

2. Materials and methods

2.1. Materials

[FeTPP(Cl)] was purchased from Strem Chemicals (Newburyport, MA, USA). Silver perchlorate, silver tetrafluoroborate, silver hexafluoroantimonate, and silver hexafluorophosphate were purchased from Aldrich (Burlington, MA, USA). All chemicals were of standard reagent grade and used as supplied. Hexane and tetrahydrofuran were also of standard reagent grade and used as supplied (Merck, Darmstadt, Germany). Dichloromethane was of spectroscopic grade and used as supplied (Merck, Darmstadt, Germany) too. FTIR grade potassium bromide (KBr) was purchased from Merck (Darmstadt, Germany).

2.2. Synthetic procedures

2.2.1. General synthetic procedure for complexes (1)–(4)

[FeTPP(Cl)] (400 mg, 0.568 mmol) was dissolved in THF (40 mL) under nitrogen atmosphere. Silver salt (1 Eq) was added and the reaction mixture was heated to 65 °C. After 5 min the reaction mixture was filtered, and hexane (11 mL) was added to the filtrate. The solution was put in the freezer for 10 days.

2.2.2. Synthesis of [FeTPP(THF)₂] $\text{ClO}_4 \cdot 2\text{THF}$ (1)

Silver perchlorate (118 mg, 0.568 mmol) was added. Crystals of (1) (482 mg; 80% yield) were collected with filtration and washed with hexane. Purple solid; DSC (10 K/min): 74.1 °C onset, 93.2 °C peak (endo), 180.2 °C onset, 188.6 °C peak (exo), 434.6 °C onset, 442.4 °C peak (endo); IR (ATR): 3438, 2975, 2873, 1596, 1479, 1440, 1334, 1200, 1070, 995 cm^{-1} .

2.2.3. Synthesis of [FeTPP(THF)(H₂O)] $\text{BF}_4 \cdot 3\text{THF}$ (2)

Silver tetrafluoroborate (111 mg, 0.568 mmol) was added. Crystals of (2) (286 mg; 47%) were collected with filtration and washed with hexane. Purple solid; DSC (10 K/min): 66.1 °C onset, 77.4 °C peak (endo), 97.6 °C onset, 104.1 °C peak (endo), 180.6 °C onset, 197.6 °C peak (endo), 155.6 °C onset, 159.7 °C peak (endo), 239.1 °C onset, 265.1 °C peak (endo); IR (ATR): 3422, 2972, 2870, 1596, 1482, 1440, 1334, 1200, 1070, 995 cm^{-1} .

2.2.4. Synthesis of [FeTPP(THF)₂] $\text{SbF}_6 \cdot 2\text{THF}$ (3)

Silver hexafluoroantimonate (195 mg, 0.568 mmol) was added. Crystals of (3) (367 mg; 54%) were collected with filtration and washed with hexane. Purple solid; DSC (10 K/min): 132.1 °C onset, 140.4 °C peak (endo), 233.1 °C onset, 240.8 °C peak (endo); IR (ATR): 3447, 2791, 2872, 1598, 1483, 1442, 1338, 1201, 1178, 1071, 1006 cm^{-1} .

2.2.5. Synthesis of [FeTPP(THF)₂] $\text{PF}_6 \cdot 2\text{THF}$ (4)

Silver hexafluorophosphate (144 mg, 0.568 mmol) was added. Crystals of (4) (253 mg; 40%) were collected with filtration and washed with hexane. Purple solid; DSC (10 K/min): 140.7 °C onset, 147.1 °C peak (endo), 152.4 °C onset, 159.4 °C peak (endo), 205.8 °C onset, 218.9 °C peak (endo), 252.8 °C onset, 276.5 °C peak (endo), 332.4 °C onset, 337.7 °C peak (endo), 431.3 °C onset, 436.9 °C peak (exo); IR (ATR): 3447, 2973, 2872, 1597, 1481, 1441, 1335, 1286, 1132, 1070, 1007 cm^{-1} .

2.2.6. Synthesis of [FeTPP(THF)Cl] · THF (5)

[FeTPP(Cl)] (400 mg, 0.568 mmol) was dissolved in THF (40 mL) under nitrogen atmosphere. The reaction mixture was heated to 65 °C. After 5 min the reaction mixture was filtered and hexane (11 mL) was added to the filtrate. The solution was put in the freezer for 10 days. Crystals of (5) (224 mg; 51%) were collected with filtration and washed with hexane. Purple solid; DSC (10 K/min): 481.0 °C onset, 483.8 °C peak (endo), 487.1 °C onset, 487.8 °C peak (endo); IR (ATR): 3435, 3109, 3023, 1829, 1596, 1485, 1440, 1333, 1200, 1174, 1069, 995 cm^{-1} .

2.3. Attenuated total reflection fourier transform infrared (ATR-FTIR) measurements

ATR-FTIR spectra were recorded on a Nicolet iS50FT-IR spectrometer (Thermo Fisher Scientific, Waltham, MA, USA) using a single reflection diamond ATR cell.

2.4. Differential scanning calorimetry (DSC) measurements

DSC thermograms were recorded on differential scanning calorimeter DSC 3⁺ Star^e System instrument (Mettler Toledo, Polaris Parkway Columbus, OH, USA) operating at 10 °C/min. Alumina pans under air

atmosphere were used.

2.5. Thermogravimetric analysis (TGA) measurements

TGA measurements were recorded on TGA/DSC 1 Star^e System (Mettler Toledo, Polaris Parkway Columbus, OH, USA) operating at 10 °C/min. Alumina pans under air atmosphere were used.

2.6. Single crystal X-ray crystallography

Single-crystal X-ray diffraction data of (2)–(5) were collected on an Agilent Technologies SuperNova Dual diffractometer using Mo-K α radiation ($\lambda = 0.71073$ Å) at 150 K. The data were processed using *CrysAlis Pro* [25]. Structures were solved by SHELXT [26] using intrinsic phasing and refined by a full-matrix least-squares procedure based on F^2 with SHELXL [27] using Olex2 program suite [28]. All the non-hydrogen atoms were refined anisotropically. Hydrogen atoms were readily located in difference Fourier maps and were subsequently treated as riding atoms in geometrically idealized positions with $U_{\text{iso}}(\text{H}) = 1.2U_{\text{eq}}(\text{C})$, except hydrogen atoms bonded to water oxygen atom in (2) that were refined restraining the O–H bond length with $U_{\text{iso}}(\text{H}) = 1.5U_{\text{eq}}(\text{O})$. In (2) two THF solvate molecules were disordered over two positions in refined ratios 0.50(2):0.50(2) and 0.63(3):0.37(3), and atoms C53, O4 and C56 as well as C57a C57b, C58 and C58b being part of two THF solvate molecules were refined restraining U^{ij} components. In (5) one THF solvate molecule was highly disordered and the electron density associated with disordered solvent molecule was removed by a solvent mask. Therefore, the chemical formula and crystal data given in Table 1 do not take into account this solvent molecule. Crystallographic data for compound (1) are in agreement with the data that has already been reported [20,21] and are therefore not presented here.

2.7. Electron paramagnetic resonance

X-band electron paramagnetic resonance (EPR) measurements were done using a Bruker Elexsys E500 EPR spectrometer operating at 9.37 GHz, equipped with a Varian TEM104 dual cavity resonator, an Oxford Instruments ESR900 cryostat, and an Oxford Instruments ITC503 temperature controller. The samples were inserted into standard 4 mm EPR quartz tubes for the purpose of the measurements. EPR spectra were measured at 4 mW microwave power and 0.2 mT modulation amplitude

with modulation frequency 80 kHz.

2.8. Magnetic susceptibility

Magnetic susceptibility of powder samples was studied in a magnetic field of 1 kOe between 2 K and 300 K using a Quantum Design MPMS-XL-5 magnetometer. The data were corrected for a temperature-independent diamagnetism, χ_{dia} , of the inner shell electrons and the sample holder.

3. Results and discussion

3.1. Synthesis of iron(III) complexes

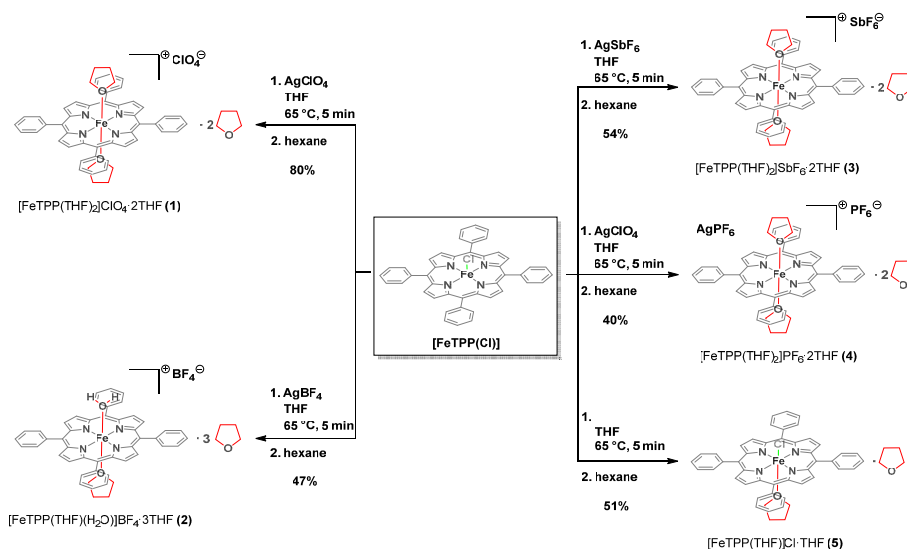
In order to study the influence of counter anions on the structural and magnetic properties of iron(III) *meso*-tetraphenylporphyrin tetrahydrofuran solvates a series of complexes were synthesized using the approach previously reported by Richter-Addo et al. [21] (Scheme 1). In short, [FeTPP(Cl)] was dissolved in THF and refluxed for 5 min with appropriate silver salt followed by addition of hexane and crystallization. The reaction of [FeTPP(Cl)] with silver perchlorate afforded [FeTPP(THF)₂]ClO₄·2THF (1) in 80% yield. The structure of (1) is identical to that previously reported in Ref. [21]. Interestingly, when [FeTPP(Cl)] was reacted in similar manner with silver tetrafluoroborate, a new complex [FeTPP(THF)(H₂O)]BF₄·3THF (2) was obtained in 47% yield. In (2) the metal center is coordinated with one water and one THF molecule instead of two THF molecules as in (1). We note that this complex is structurally close to known [FeTPP(THF)₂]BF₄ [23]. The incorporation of the water into the complex is surprising and probably originates from the water present in the inorganic salt, since the same lot of anhydrous THF solvent was used for all experiments. In the case of reaction of silver hexafluoroantimonate with [FeTPP(Cl)], we isolated complex [FeTPP(THF)₂]SbF₆·2THF (3) in 54% yield, which contains an extra THF compared to [FeTPP(THF)₂]SbF₆·THF [21]. Treatment of [FeTPP(Cl)] with hexafluorophosphate provided [FeTPP(THF)₂]PF₆·2THF (4) in 40% yield. Finally, when [FeTPP(Cl)] was simply refluxed in THF, a new complex (5) was isolated in 51% yield (Scheme 1). All samples were first extensively characterized by attenuated total reflectance Fourier transform infrared spectroscopy (Figs. S1.1-S1.5) and thermal analysis (Figs. S2.1-S2.5) [29].

Table 1
Crystallographic data for (2)–(5).

	(2)	(3)	(4)	(5)
CCDC number	2247176	2247177	2247178	2247179
Formula	C ₆₀ H ₆₂ BF ₄ FeN ₄ O ₅	C ₆₀ H ₆₀ F ₆ FeN ₄ O ₄ Sb	C ₆₀ H ₆₀ F ₆ FeN ₄ O ₄ P	C ₄₈ H ₃₆ ClFeN ₄ O
M_r	1061.79	1192.72	1101.94	776.11
T (K)	150.00(10)	150.00(10)	150.00(10)	150.00(10)
Crystal system	monoclinic	tetragonal	tetragonal	monoclinic
Space group	$P2_1/c$	$P4_12_12$	$P4_12_12$	$P2_1/n$
a (Å)	13.8721(5)	17.0980(5)	16.9476(5)	11.1120(4)
b (Å)	17.2844(6)	17.0980(5)	16.9476(5)	19.5956(6)
c (Å)	22.3076(8)	18.6920(9)	18.5940(10)	19.5107(6)
β (°)	99.930(3)	90	90	92.173(3)
Volume (Å ³)	5268.6(3)	5464.4(4)	5340.6(4)	4245.3(2)
Z	4	4	4	4
D_c (g/cm ³)	1.339	1.450	1.370	1.214
μ (mm ⁻¹)	0.355	0.831	0.385	0.457
$F(000)$	2228	2444	2300	1612
Reflections collected	27976	17551	15963	21261
Data/restraints/parameters	12065/18/711	6261/0/347	6117/0/347	9734/0/496
R_{int}	0.0304	0.0338	0.0341	0.0269
R , wR_2 [$I > 2\sigma(I)$] ^a	0.0626, 0.1664	0.0744, 0.1526	0.0425, 0.0961	0.0642, 0.1653
R , wR_2 (all data) ^a	0.0904, 0.1917	0.0903, 0.1593	0.0653, 0.1070	0.0772, 0.1753
GOF, S^b	1.036	1.295	1.021	1.030
$\Delta\rho_{\text{max}}$, $\Delta\rho_{\text{min}}$ (e Å ⁻³)	1.40/−0.84	1.01/−1.23	0.31/−0.25	2.16/−0.53
Flack parameter	/	0.031(11)	−0.001(9)	/

^a $R = \sum ||F_o| - |F_c|| / \sum |F_o|$, $wR_2 = \{\sum [w(F_o^2 - F_c^2)^2] / \sum [w(F_o^2)^2]\}^{1/2}$.

^b $S = \{\sum [(F_o^2 - F_c^2)^2 / (n/p)]^{1/2}\}^{1/2}$, where n is the number of reflections and p is the total number of refined parameters.



Scheme 1. Preparation of complexes (1)–(5) from the parent [FeTPP(Cl)] complex.

3.2. Structural properties

Compounds (2) and (5) crystallize in the monoclinic space group $P2_1/c$ and $P2_1/n$, respectively, with all of the atoms located in general positions. Compounds (3) and (4) crystallize in the tetragonal space group $P4_12_12$ and the asymmetric units are composed of half of [FeTPP(THF)₂]⁺ cation, half of SbF₆⁻ or PF₆⁻ anion and one THF molecule with iron(III) metal center as well as Sb and P atoms positioned on the two-fold rotation axis. The iron(III) metal center is in an octahedral coordination geometry in the equatorial plane formed by the porphyrin nitrogen atoms in (3) and (4) while in (2) and (5) it is slightly above the plane (0.038 and 0.260 Å, respectively). The Fe–N distances 2.024(3) and 2.038(4) Å for (3) and 2.026(3) and 2.027(4) Å for (4) are slightly shorter than distances in the range 2.035(2)–2.049(2) Å for (2) and 2.044(2)–2.053(2) Å for (5) (Figs. 1–3, S3.1, Tables 2–4).

The axial positions in (2)–(5) consist of different ligands. Axial positions in (2) are occupied by one water and one THF molecule, in (3) and (4) by two THF molecules and in (5) by one chloride ligand and one THF molecule (Figs. 1–3, S3.1). The presence of different axial ligands

causes differences in Fe–L_{axial} bond lengths. The Fe–O_{THF} distances of 2.1768(19) Å in (2), 2.137(6) Å in (3) and 2.134(2) Å in (4) are similar as in [FeTPP(THF)₂ClO₄] [21], while in (5) the Fe–O_{THF} distance of 2.442(2) Å is significantly elongated compared to complexes (2)–(4) (Tables 2–4). The Fe–O_w distance of 2.042(2) Å in (2) is somewhat shorter than previously observed in [FeTPP(H₂O)₂]ClO₄ (2.130(3) Å) [2]. In (5) the Fe–Cl distance is 2.2569(8) Å. We note that in mononuclear compounds with two chloride ligands in the axial position Fe–Cl distances are in the range 2.425–2.431 Å [30,31]. In the case of mixed axial ligands Fe–Cl distance is 2.305 Å or 2.514 Å with methanol or acetate ligand in *trans* position, respectively [32,33]. In penta-coordinated Fe-porphyrin compounds the observed Fe–Cl distance is 2.220 Å in [FeTPP(Cl)] [34] and slightly elongated distances are present in *meso*-tetraethyl or *meso*-tetraisopropylporphyrin complexes (2.264 and 2.238 Å, respectively) [35,36]. Slight distortion of octahedral geometry in (2)–(4) can be seen since O–Fe–O, *trans* N–Fe–N and *cis* N–Fe–N angles deviate from ideal values only to a minor degree (Tables 2 and 3). Moderate distortion in (5) is indicated by, for example, *trans* N–Fe–N angles of 164.87(9) and 165.97(9)° (Table 3). The shortest

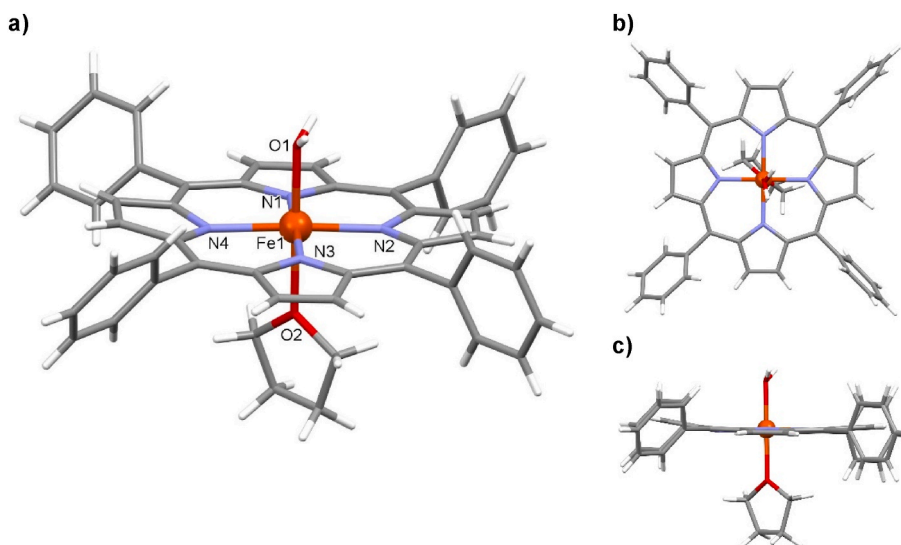


Fig. 1. Perspective drawing (a) and top (b) and side (c) views of the cationic mononuclear iron(III) unit of (2).

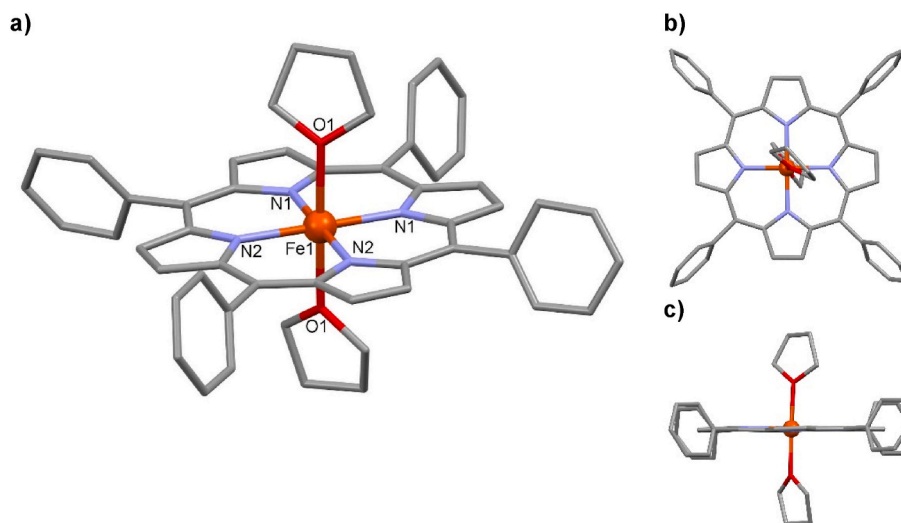


Fig. 2. Perspective drawing (a) and top (b) and side (c) views of the cationic mononuclear iron(III) unit of (3). Drawings for (4) are in Ref. [29]. Hydrogen atoms have been omitted for clarity.

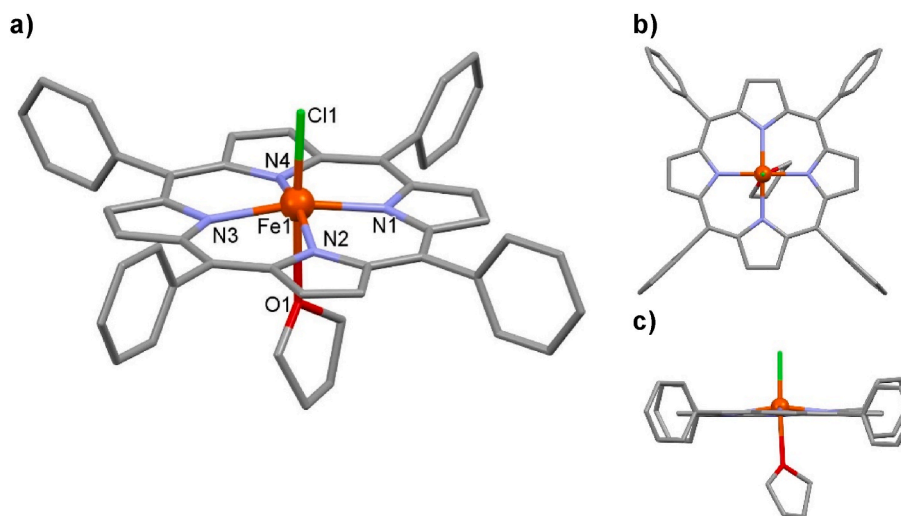


Fig. 3. Perspective drawing (a) and top (b) and side (c) views of (5). Hydrogen atoms have been omitted for clarity.

Table 2
Selected bond distances (Å) and angles (°) for (2).

Distance (Å)			
Fe1–O1	2.042(2)	Fe1–N2	2.046(2)
Fe1–O2	2.1768(19)	Fe1–N3	2.035(2)
Fe1–N1	2.040(2)	Fe1–N4	2.049(2)
Angle (°)			
O1–Fe1–O2	179.47(8)	O2–Fe1–N4	89.28(8)
O1–Fe1–N1	90.97(9)	N1–Fe1–N2	89.98(9)
O1–Fe1–N2	91.95(9)	N1–Fe1–N3	178.51(9)
O1–Fe1–N3	90.51(9)	N1–Fe1–N4	89.79(8)
O1–Fe1–N4	90.78(9)	N2–Fe1–N3	90.14(9)
O2–Fe1–N1	89.55(8)	N2–Fe1–N4	177.27(9)
O2–Fe1–N2	88.00(8)	N3–Fe1–N4	90.02(8)
O2–Fe1–N3	88.96(8)		

Fe...Fe intermolecular distance between adjacent iron(III) metal centers in (2)–(5) are 10.448, 10.486, 10.434 and 9.854 Å, respectively.

In (2) coordinated water molecule forms O–H...O hydrogen bonding with THF solvate molecule and a bifurcated O–H...F hydrogen bonding

Table 3
Selected bond distances (Å) and angles (°) for (3) and (4).

	(3)	(4)
Distance (Å)		
Fe1–O1	2.137(6)	2.134(2)
Fe1–N1	2.021(7)	2.027(3)
Fe1–N2	2.032(7)	2.026(3)
Angle (°)		
O1–Fe1–O1 ⁱ	177.2(4)	177.74(14)
O1–Fe1–N1	88.1(3)	91.09(10)
O1–Fe1–N1 ⁱ	90.0(3)	90.49(10)
O1–Fe1–N2	90.3(3)	89.94(10)
O1–Fe1–N2 ⁱ	91.6(3)	88.48(10)
N1–Fe1–N1 ⁱ	89.8(5)	90.86(17)
N1–Fe1–N2	89.5(3)	89.19(11)
N1–Fe1–N2 ⁱ	179.2(4)	179.57(11)
N2–Fe1–N2 ⁱ	91.2(5)	90.76(16)

Symmetry code for 3: (i) y, x, 1 – z; for 4: (i) 1 – y, 1 – x, 3/2 – z.

Table 4
Selected bond distances (Å) and angles (°) for (5).

Distance (Å)			
Fe1–O1	2.442(2)	Fe1–N2	2.044(2)
Fe1–Cl1	2.2569(8)	Fe1–N3	2.055(2)
Fe1–N1	2.053(2)	Fe1–N4	2.053(2)
Angle (°)			
O1–Fe1–Cl1	177.34(5)	Cl1–Fe1–N4	97.36(6)
O1–Fe1–N1	81.53(8)	N1–Fe1–N2	89.63(8)
O1–Fe1–N2	81.44(8)	N1–Fe1–N3	165.97(9)
O1–Fe1–N3	84.45(8)	N1–Fe1–N4	89.09(8)
O1–Fe1–N4	83.46(8)	N2–Fe1–N3	88.88(9)
Cl1–Fe1–N1	95.95(6)	N2–Fe1–N4	164.87(9)
Cl1–Fe1–N2	97.76(6)	N3–Fe1–N4	88.71(9)
Cl1–Fe1–N3	98.08(6)		

with BF_4^- anion. These interactions are supported by C–H...F hydrogen bonding between a phenyl group of the complex cation and BF_4^- anion (Fig. 4, Table 5). A zig-zag chain along *c* axis is formed through C–H...F interaction between a phenyl group of the adjacent complex cation with the BF_4^- anion.

In (3) and (4), each SbF_6^- and PF_6^- anion, respectively, is involved in C–H...F interactions as hydrogen-bond acceptor with four adjacent complex cations (Fig. 5 and S3.2, Table 5). In (5) no significant hydrogen-bonding interactions are present.

3.3. Magnetic properties

Temperature-dependent molar magnetic susceptibilities, χ_m , measured in the temperature range between 2 K and 300 K for powder samples of $[\text{Fe}^{\text{III}}\text{TPP}(\text{THF})_2]\text{ClO}_4 \cdot 2\text{THF}$, $[\text{Fe}^{\text{III}}\text{TPP}(\text{THF})(\text{H}_2\text{O})]\text{BF}_4 \cdot 3\text{THF}$, $[\text{Fe}^{\text{III}}\text{TPP}(\text{THF})_2]\text{SbF}_6 \cdot 2\text{THF}$ and $[\text{Fe}^{\text{III}}\text{TPP}(\text{THF})_2]\text{PF}_6 \cdot 2\text{THF}$ with ClO_4^- , BF_4^- , SbF_6^- , PF_6^- as counter anions and Cl^- as an axial ligand in $[\text{FeTPP}(\text{THF})(\text{Cl})] \cdot \text{THF}$ show in all cases a strong paramagnetic response without any signatures of cooperative magnetic phenomena (Figure S4.1). After subtracting the temperature-independent diamagnetic contribution, χ_{dia} , from χ_m , the effective magnetic moment, μ_{eff} , per Fe site is evaluated from the high-temperature value of the product $\sqrt{\chi_m T}$. The effective magnetic moment ranges between $\mu_{\text{eff}} = 5.82$ for Cl^- and $\mu_{\text{eff}} = 6.26$ for BF_4^- samples, respectively. These values are close to the spin-only value anticipated for the high-spin $S = 5/2$ state of iron (III) and are similar to those experimentally found for the other penta- and hexa-coordinated iron(III) centers in porphyrins with axial halides [32]. We note though that the variations in the extracted μ_{eff} values between different samples are non-negligible and can be ascribed to the dependence of the iron(III) *g*-factor values on the spin–orbit coupling (SOC) with the axial ligand group.

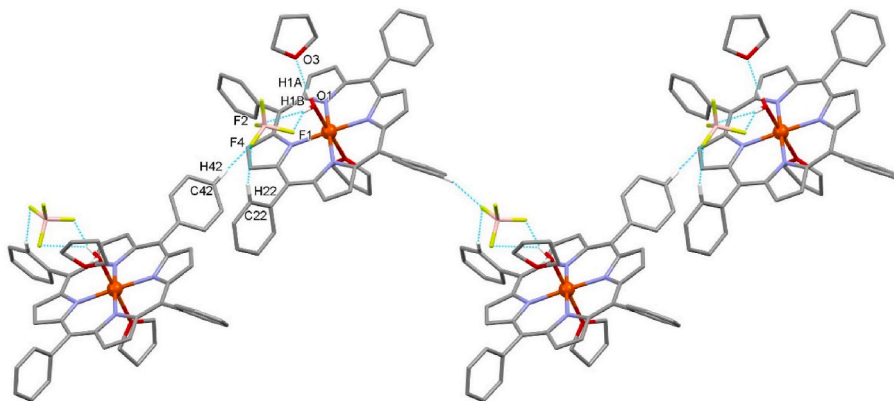


Fig. 4. Hydrogen-bond chain along *c* axis in (2). Hydrogen bonds are represented by dashed blue lines. Two THF molecules, a disorder on hydrogen-bonded THF molecule, and hydrogen atoms not involved in the motif shown have been omitted for clarity.

Table 5
Hydrogen bonds for (2)–(4) [Å and °].

D–H...A	<i>d</i> (D–H)	<i>d</i> (H...A)	<i>d</i> (D...A)	<(DHA)
(2)				
O1–H1a...O3	0.836(18)	1.798(19)	2.632(3)	175(4)
O1–H1b...F1	0.844(18)	1.93(2)	2.730(3)	158(3)
O1–H1b...F2	0.844(18)	2.46(3)	3.135(5)	137(3)
C22–H22...F4	0.95	2.51	3.426(4)	162
C42–H42...F4 ⁱ	0.95	2.44	3.362(5)	164
(3)				
C1–H1...F1 ⁱⁱ	0.95	2.46	3.303(14)	148
C16–H16...F2 ⁱ	0.95	2.39	3.300(16)	161
C29–H29A...F2	0.99	2.53	3.17(2)	121
C25–H25...F3 ^{iv}	0.95	2.54	3.387(13)	148
(4)				
C1–H1...F1 ⁱⁱ	0.95	2.49	3.365(4)	153
C12–H12...F2	0.95	2.54	3.442(5)	159
C25–H25...F3 ⁱⁱⁱ	0.95	2.47	3.338(4)	153

Symmetry codes for 2: (i) $x, 3/2 - y, 1/2 + z$; for 3: (i) $y, x, 1 - z$; (ii) $-1/2 + y, 1/2 - x, -1/4 + z$; (iii) $1/2 + y, 3/2 - x, -1/4 + z$; for 4: (ii) $1/2 - y, 1/2 + x, 1/4 + z$; (iii) $3/2 - y, -1/2 + x, 1/4 + z$.

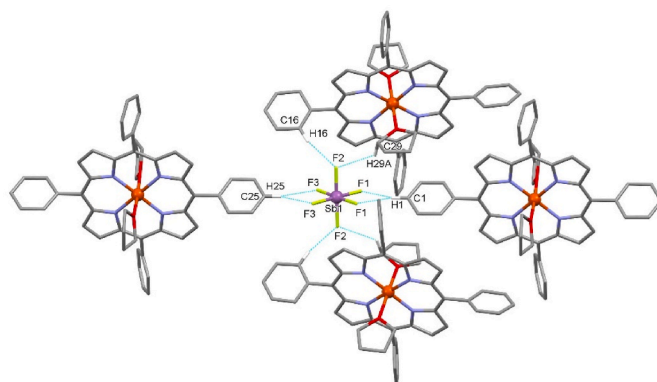


Fig. 5. Hydrogen-bonding interactions of SbF_6^- with adjacent cationic mononuclear iron(III) unit of (3). Drawing for (4) is in Ref. [29]. Hydrogen atoms not involved in the motif shown have been omitted for clarity.

Below ~ 50 K, $\mu_{\text{eff}}(T)$ starts to decrease on cooling for all samples, which is a hallmark of a sizeable zero-field splitting. In order to extract the axial ZFS parameter *D*, we start with the minimal spin Hamiltonian $H = \mu_B \mathbf{B} g \hat{S} + D(\hat{S}_z^2 + S(S+1)/3)$ and fit the temperature dependence of $\mu_{\text{eff}}(T)$ by using the Easyspin package [37] with *D* and axial *g*-factor as the only free parameters. This approach yields satisfactory agreement for all samples (Fig. 6) and the summary of extracted ZFS parameter *D*

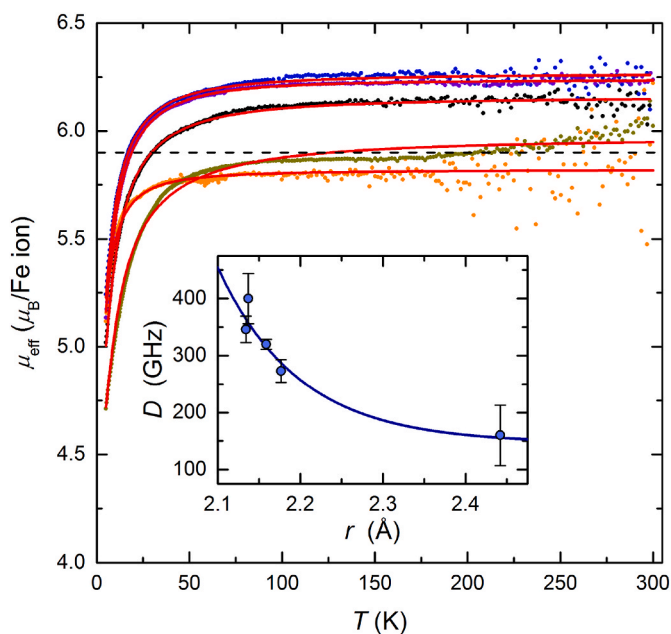


Fig. 6. Temperature dependences of the effective magnetic moments, μ_{eff} , for [FeTPP(THF)]X powder samples with counter anions X = ClO_4^- (1) (purple circles), X = BF_4^- (2) (blue circles), X = SbF_6^- (3) (green circles), X = PF_6^- (4) (black circles) and axial ligand Cl^- (5) (orange circles). Solid red lines represent simulations with a model based on an axial ZFS system. The dashed horizontal line marks the expected value for the high spin $S = 5/2$ Fe moment with isotropic $g = 2.0023$. The inset shows extracted ZFS parameter D in relation to the iron(III) – THF oxygen atom distance, r . The blue line in the inset is a guide to the eye.

values from the magnetic susceptibility data is given in Table 6. The values of $D \approx 160 \text{ GHz} - 400 \text{ GHz}$ ($= 5.3 \text{ cm}^{-1} - 13.34 \text{ cm}^{-1}$) are in the range found for various [Fe^{III}TPP(X)] complexes [16,17,38]. Even though the ZFS parameter values extracted from the spin susceptibility data are known to be less accurate [17], a comparison between samples with similar counter anions, shows some important trends. The sample with Cl^- that axially coordinates to [Fe^{III}TPP(THF)] species has significantly lower $D = 5.3 \text{ cm}^{-1}$ compared to other samples with axially coordinated THF molecules and non-coordinating counter ions. For cases when axial ligands are changed, variations in D may be due to partial spin delocalization onto the axial ligand groups that determines the degree of their spin-orbit coupling contribution to ZFS [17]. On the other hand, when axial ligands are kept the same and only non-coordinating anions are varied, we still observe variations in D . For example, for the X = BF_4^- (2) and PF_6^- (4) samples, D increases from 9.11 cm^{-1} to 11.54 cm^{-1} (Table 6), respectively.

A complementary insight into the magnetic anisotropies of [FeTPP(THF)]X samples can be obtained from the EPR spectra. A very broad X-band EPR signal with effective g -factor values $g_{\perp} \approx 6$ and $g_{\parallel} \approx 2$ can be found for all polycrystalline samples at room temperature. These g -factor values are characteristic of high-spin $S = 5/2$ iron(III) centers showing large axial ZFS parameter D . In order to interpret EPR spectra

Table 6

Extracted values of the ZFS parameter D from the magnetic susceptibility data for the different samples and their relation to Fe – O_{THF} distance. *Average Fe – $\text{O}_1(2)$ distance is taken from Ref. [21].

Sample/counter anion	Fe – O_{THF} distance [Å]	D [GHz]	D [cm^{-1}]
(1)/ ClO_4^-	2.1585*	320	10.67
(2)/ BF_4^-	2.1768	273	9.11
(3)/ SbF_6^-	2.137	400	13.34
(4)/ PF_6^-	2.134	346	11.54
(5)/none (axial Cl^-)	2.442	160	5.34

we thus proceed with the model of a spin system consisting of $S = 5/2$ spin and including axial anisotropy in the g -factor (i.e., the Fe^{III}TPP in-plane eigen-value is g_{\perp} and out-of-plane is g_{\parallel}) and the ZFS anisotropy with the axial and rhombic parameters D and E (Equation (1)) [39]:

$$H_{\text{EPR}} = \mu_{\text{B}} \mathbf{B} g \hat{S} + D(\hat{S}_z^2 + S(S+1)/3) + E(\hat{S}_x^2 - \hat{S}_y^2). \quad (1)$$

Here we neglect the residual small anisotropy in g -factor in the Fe^{III}TPP plane and co-align the main eigenaxes of the g -factor and ZFS anisotropy tensors. The axial ZFS parameter D significantly influences the positions of EPR lines only when its magnitude is comparable to the applied microwave frequency [38]. From the above analysis of χ_{m} we conclude that the values of D are indeed much larger compared to the microwave frequency (Larmor frequency is in these experiments $\nu_{\text{L}} = 9.37 \text{ GHz}$). Therefore, we proceed by fixing the axial ZFS parameter D values to those obtained from the magnetic susceptibility measurements (Table 6). On the other hand, variations in rhombic ZFS parameter E have a more pronounced effect on the positions of the resonances even when $D \gg \nu_{\text{L}}$. We therefore proceed with EPR lineshape simulations to determine this parameter too. Finally, a Gaussian line broadening, ΔB , is used for all calculated EPR spectra, as the main source of broadening is due to the dipolar interactions between neighboring iron(III) spins. This last assumption agrees well with the negligible exchange interactions (inset to Fig. S4.1) because of the large distances between nearest neighboring iron(III) spins, being around 10 Å .

At $T = 150 \text{ K}$, X-band EPR spectra remain qualitatively similar to those measured at room temperature except for the reduced ΔB [Fig. 7 (a)]. We thus simulate X-band EPR spectra measured at $T = 150 \text{ K}$ using the model of Eq. (1) as it allows us a more precise determination of anisotropy parameters (Table 7). From the X-band EPR spectral simulations we notice a significant axial anisotropy in the g -factor, which corresponds well to the axial nature of the ZFS. Most importantly, these EPR simulations yield very small, effectively zero values for the rhombic ZFS parameter E . Namely, increasing the value of E/D would in the X-band EPR spectra split and shift the strong signal at effective $g_{\perp} \approx 6$ (Figure S4.2), which has not been observed in the experiment. The observations that $E \rightarrow 0$ corroborate the structural data taken at $T = 150 \text{ K}$, which show almost perfect iron(III) axial symmetry displaying only small porphyrin plane distortions and some minor tilting of the THF molecules. Such small structural distortions in principle give rise to minor rhombicity effects, but they are here clearly too small to have an observable effect on the X-band EPR spectra at 150 K .

On further cooling [FeTPP(THF)]X samples to $T = 20 \text{ K}$, the X-band EPR spectra continue to narrow down as ΔB decreases to $\approx 20 \text{ mT}$. This allows us to monitor fine shifts and splitting of EPR spectra, in particular the spectral part around the effective $g_{\perp} \approx 6$. Moreover, we notice the appearance of several additional weaker peaks in the EPR spectra [Fig. 7 (b)]. These spectral features disclose the lowering of the iron(III) symmetry at these cryogenic temperatures where more pronounced rhombicity distortions increase the rhombic ZFS parameter E . Attempts to simulate such complex powder spectra with a single component mostly failed, since the Hamiltonian (Eq. (1)) cannot reproduce the fine structure of a strong effective $g_{\perp} \approx 6$ signal that is at the same time flanked by several weaker resonances. We thus conclude that at least two components with slightly different sets of spin parameters are needed, where some of the iron(III) spins retain the approximate axial symmetry, while the others change to a more rhombic environment. The complete set of parameters for the $T = 20 \text{ K}$ EPR spectra simulations [Fig. 7(b)] with a two-component model are given in the second part of Table 7.

The two-component model indeed captures fine structure of the main peak around effective $g_{\perp} \approx 6$ for samples (1) and (2). The ratios of the intensities for the two components are approximately 1:1, which may hint a possible low-temperature structural change with the doubling of the unit cell. On the other hand, the EPR spectrum of sample (4) can be accounted for by a single component. Finally, samples (3) and (5) show even more rich X-band EPR spectra, that the simple spin Hamiltonian

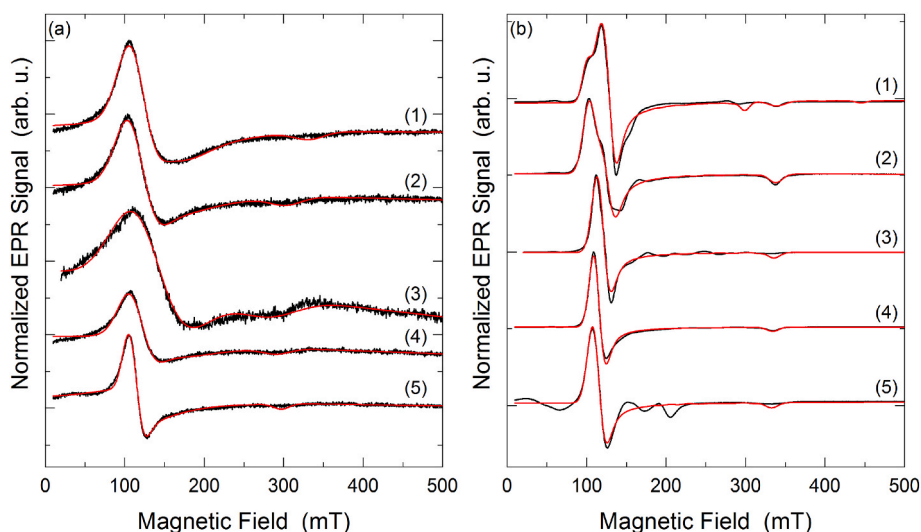


Fig. 7. X-band EPR spectra of polycrystalline $[\text{FeTPP}(\text{THF})]\text{X}$ samples ($\text{X} = \text{ClO}_4^-$ (1), BF_4^- (2), SbF_6^- (3) and PF_6^- (4)) and $[\text{FeTPP}(\text{THF})(\text{Cl})]$ (5) measured at $T = 150$ K (a) and $T = 20$ K (b). The solid red lines are powder spectrum simulations for high-spin $S = 5/2$ ZFS system of the model represented by Eq. (1) using Easyspin code [37].

Table 7

Results from simulations of powder X-band EPR spectra to Eq. (1). When two sets of parameters are given, a two-component simulation has been applied. In all cases the ZFS parameter D was in Eq. (1) fixed to values obtained from the magnetic susceptibility data simulations (Table 6).

Sample/counter anion	$T = 150$ K				$T = 20$ K			
	g_{\perp}	g_{\parallel}	ΔB [mT]	E [GHz]	g_{\perp}	g_{\parallel}	ΔB [mT]	E [GHz]
(1)/ ClO_4^-	1.9318	2.0119	42.4	0.022	1.8203	1.9765	20.7	0.200
(2)/ BF_4^-	1.9550	2.2049	44.3	0.050	1.9736	2.2731	13.8	11.60
					1.8059	1.9727	19.9	0.050
(3)/ SbF_6^-	1.7346	2.3500	79.9	0.036	2.0793	1.9727	20.0	0.050
					1.8979	1.9864	17.9	2.500
(4)/ PF_6^-	1.9475	2.2941	39.2	0.083	1.9762	2.0004	16.4	0.227
					1.9898	2.0007	18.9	0.022
(5)/none (axial Cl^-)	2.0162	2.2416	22.3	0.020				

Eq. (1) with two components included cannot reproduce. Possible explanations for this disagreement would necessitate further structural distortions, such as (i) low-temperature distortions of the crystal structure with the larger unit cell and crystallographic splitting of iron(III) sites, or (ii) chemical and structural inhomogeneities of polycrystalline samples employed in this study. A source for such inhomogeneities could be the gradual loss of THF solvent molecules from parts of the sample. A detailed structural investigation conducted at low temperatures is needed to address the appearance of additional fine structure EPR features that cannot be accounted for by Eq. (1) and complementary high-field EPR measurements would be needed to extract more accurate D and E values.

Combined magnetic susceptibility and X-band EPR measurements on samples (1)-(5) showed that ZFS anisotropy varies not only when axial ligand is changed, but also when counter anion is varied. The observed correlation between the different non-coordinating counter ions and the magnetic anisotropies is at first sight surprising as there is no direct interaction between hexa-coordinated iron(III) and non-coordinating anions. As can be deduced from the structural data described in Section 3.1, different counter anions have a measurable effect on the distance between the iron(III) and the oxygen atoms of the THF axial ligand. Specifically, the extracted values of the axial ZFS parameter D increase with decreasing iron(III) to oxygen atom distance thus revealing a clear correlation between the magnetic properties and the precise location of the axial THF ligands (inset to Fig. 6 and Table 6). A qualitative explanation for such behavior can be given within the ligand field theory as outlined for FeTPP in Ref. [11] or [17]. Within this model, the tetragonal elongation of the iron(III) geometry yields a positive sign for D . The value of D will increase if the energy of the

excited 4A_2 state (i.e., $d_{xy}^2 d_{yz}^1 d_{xz}^1 d_{z^2}^1$) decreases and/or when the 4E state (i.e., $d_{xy}^1 d_{yz}^1 d_{xz}^2 d_{z^2}^1 / d_{xy}^1 d_{yz}^2 d_{xz}^1 d_{z^2}^1$) increases in energy. The presence of counter anion affects the axial THF ligand by changing its bonding energy and the iron(III)-oxygen distance. As a result, it also tunes 4A_2 and 4E energies and the resulting D .

4. Conclusions

In conclusion, we have reproduced $[\text{FeTPP}(\text{THF})_2]\text{ClO}_4 \cdot 2\text{THF}$ as well as synthesized novel $[\text{FeTPP}(\text{THF})(\text{H}_2\text{O})]\text{BF}_4 \cdot 3\text{THF}$, $[\text{FeTPP}(\text{THF})_2]\text{SbF}_6 \cdot 2\text{THF}$, and $[\text{FeTPP}(\text{THF})_2]\text{PF}_6 \cdot 2\text{THF}$ compounds with ClO_4^- , BF_4^- , SbF_6^- , PF_6^- acting as counter anions and $[\text{FeTPP}(\text{THF})(\text{Cl})] \cdot \text{THF}$ with Cl^- as the axial ligand. The choice of anions (ClO_4^- , BF_4^- , SbF_6^- , PF_6^- , Cl^-) is used to tune the distance between the coordinated iron(III) and the oxygen atom of the axial THF ligand molecule. The shortest Fe– O_{THF} distance of 2.134(2) and 2.137(6) Å was observed in (4) and (3), respectively, while in (2) and (5) this distance was found to be 2.1768 (19) and 2.442(2) Å, respectively. We find that the elongation of this distance plays a major role in reducing the relevant ZFS parameter D , which is discussed within the ligand field theory. However, the effect of water in compound (2) and chloride in (5) as axial ligands should not be neglected. Nevertheless, the distance Fe–O(THF) is still a very sensitive parameter of local Fe coordination and thus a meaningful measure for the magnetic anisotropy. When designing molecular magnets $[\text{FeTPP}(\text{THF})_x]\text{X}$ one thus has an additional mean to control its magnetic anisotropy: with the choice of non-coordinating counter anion a fine variation in D can be achieved via stretching the iron(III)-oxygen distance.

Credit authors statement

T. Knaflič: performed EPR measurements, simulated magnetic susceptibility and EPR data and discussed magnetic properties.

M. Znidarič: synthesized and characterized samples.

F. Perdih: performed XRD measurements and refined structures.

M. Trampuž: synthesized and characterized samples.

Z. Jagličič: measured magnetic susceptibilities and discussed magnetic properties.

Z. Časar: conceived, developed and supervised the work.

D. Arčon: conceived, developed and supervised the work.

All authors contributed to the interpretation of the data and editing of the manuscript.

Declaration of competing interest

The authors declare that they have no known competing financial interests or personal relationships that could have appeared to influence the work reported in this paper.

Data availability

Data will be made available on request.

Acknowledgement

The authors acknowledge Mrs. Helena Cimerman from Lek d.d. for her assistance in acquisition of FTIR spectra and DSC and TGA thermograms. We thank the EN-FIST Centre of Excellence, Ljubljana, Slovenia, for the use of their SuperNova diffractometer. D.A. acknowledges financial support from the Slovenian Research Agency (Core Research Funding No. P1-0125). Z.J. acknowledges financial support from the Slovenian Research Agency (P2-0348). A part of this research, performed at Lek d.d., was conducted under the Novartis Genesis Labs project (Cohort Three).

Appendix A. Supplementary data

Supplementary data to this article can be found online at <https://doi.org/10.1016/j.jpcs.2023.111514>.

References

- [1] D. Zhang, W. Lan, Z. Zhou, L. Yang, Q. Liu, Y. Bian, J. Jiang, Manganese(III) porphyrin-based magnetic materials, *Top. Curr. Chem.* 377 (2019) 18, <https://doi.org/10.1007/s41061-019-0244-5>.
- [2] M. Viciano-Chumillas, G. Blondin, M. Clémancey, J. Krzystek, M. Ozerov, D. Armentano, A. Schnegg, T. Lohmiller, J. Telsler, F. Lloret, J. Cano, Single-ion magnetic behaviour in an iron(III) porphyrin complex: a dichotomy between high spin and 5/2–3/2 spin admixture, *Chem. Eur. J.* 26 (2020) 14242–14251, <https://doi.org/10.1002/chem.202003052>.
- [3] F.A. Walker, NMR and EPR spectroscopy of paramagnetic metalloporphyrins and heme proteins, in: *Handbook of Porphyrin Science*, World Scientific Publishing Company, 2010, pp. 1–337, https://doi.org/10.1142/9789814307246_0001.
- [4] A.J. Epstein, C.M. Wynn, M.A. Girtu, W.B. Brinckerhoff, K.-I. Sugiura, J.S. Miller, Magnetic ground state and its control in porphyrin-based magnets, molecular crystals and liquid crystals science and technology, *Mol. Cryst. Liq. Cryst. A* 305 (1997) 321–332, <https://doi.org/10.1080/10587259708045069>.
- [5] M. Balanda, K. Falk, K. Griesar, Z. Tomkowicz, W. Haase, Characterization of magnetic ordering in porphyrin-based molecular magnets [Mn(R)₄TPP][TCNE] (R=OC₁₂H₂₅, F, CN), *J. Magn. Magn. Mater.* 205 (1999) 14–26, [https://doi.org/10.1016/S0304-8853\(99\)00454-0](https://doi.org/10.1016/S0304-8853(99)00454-0).
- [6] J.S. Miller, J.C. Calabrese, R.S. McLean, J. A. Epstein, meso-(tetraphenylporphyrinato)manganese(III)-tetracyanoethenide, [mn^{III}TPP]²⁺ [TCNE]²⁻. A new structure-type linear-chain magnet with a Tc of 18K, *Adv. Mater.* 4 (1992) 498–501, <https://doi.org/10.1002/adma.19920040710>.
- [7] A. Kajiwarra, A. Takamizawa, T. Yamaguchi, W. Mori, K. Yamaguchi, M. Kamachi, Magnetic properties of polymers containing paramagnetic metalloporphyrins in their main chain, molecular crystals and liquid crystals science and technology, *Mol. Cryst. Liq. Cryst. A* 306 (1997) 25–32, <https://doi.org/10.1080/10587259708044545>.
- [8] S.C. Hunter, A.A. Podlesnyak, Z.-L. Xue, Magnetic excitations in metalloporphyrins by inelastic neutron scattering: determination of zero-field splittings in iron, manganese, and chromium complexes, *Inorg. Chem.* 53 (2014) 1955–1961, <https://doi.org/10.1021/ic4028354>.
- [9] G. Harris, Zero-field splitting, magnetic-field energies, effective magnetic moments, and electric-field gradients in high-spin ferric porphyrin compounds, *J. Chem. Phys.* 48 (1968) 2191–2214, <https://doi.org/10.1063/1.1669413>.
- [10] H. Goff, L.O. Morgan, Magnetic properties of iron(III) porphyrin dimers in aqueous solution, *Inorg. Chem.* 15 (1976) 3180–3181, <https://doi.org/10.1021/ic50166a054>.
- [11] J. Telsler, EPR interactions – zero-field splittings, in: *EMagRes*, John Wiley & Sons, Ltd, 2017, pp. 207–234, <https://doi.org/10.1002/9780470034590.emrstm1501>.
- [12] G.C. Brackett, P.L. Richards, W.S. Caughey, Far-infrared magnetic resonance in Fe(III) and Mn(III) porphyrins, myoglobin, hemoglobin, ferrichrome A, and Fe(III) dithiocarbamates, *J. Chem. Phys.* 54 (1971) 4383–4401, <https://doi.org/10.1063/1.1674688>.
- [13] C.A. Reed, T. Mashiko, S.P. Bentley, M.E. Kastner, W.R. Scheidt, K. Spartaian, G. Lang, The missing heme spin state and a model for cytochrome c'. The mixed S = 3/2, 5/2 intermediate spin ferric porphyrin: perchlorato(meso-tetraphenylporphyrinato)iron(III), *J. Am. Chem. Soc.* 101 (1979) 2948–2958, <https://doi.org/10.1021/ja00505a023>.
- [14] C.A. Reed, F. Guiset, A “magnetochemical” series. Ligand field strengths of weakly binding anions deduced from S = 3/2, 5/2 spin state mixing in iron(III) porphyrins, *J. Am. Chem. Soc.* 118 (1996) 3281–3282, <https://doi.org/10.1021/ja954263i>.
- [15] R. Birdy, D.V. Behere, S. Mitra, Magnetic properties and electronic structure of high spin iron(III) porphyrins, *J. Chem. Phys.* 78 (1983) 1453–1458, <https://doi.org/10.1063/1.444888>.
- [16] S.E. Stavretis, M. Atanasov, A.A. Podlesnyak, S.C. Hunter, F. Neese, Z.-L. Xue, Magnetic transitions in iron porphyrin halides by inelastic neutron scattering and ab initio studies of zero-field splittings, *Inorg. Chem.* 54 (2015) 9790–9801, <https://doi.org/10.1021/acs.inorgchem.5b01505>.
- [17] P. Tin, S.E. Stavretis, M. Ozerov, J. Krzystek, A.N. Ponomaryov, S.A. Zvyagin, J. Wosnitza, C.-C. Chen, P.P.-Y. Chen, J. Telsler, Z.-L. Xue, Advanced magnetic resonance studies of tetraphenylporphyrinatoiron(III) halides, *Appl. Magn. Reson.* 51 (2020) 1411–1432, <https://doi.org/10.1007/s00723-020-01236-8>.
- [18] A.N. Bone, S.E. Stavretis, J. Krzystek, Z. Liu, Q. Chen, Z. Gai, X. Wang, C.A. Steren, X.B. Powers, A.A. Podlesnyak, X.-T. Chen, J. Telsler, H. Zhou, Z.-L. Xue, Manganese tetraphenylporphyrin bromide and iodide. Studies of structures and magnetic properties, *Polyhedron* 184 (2020), 114488, <https://doi.org/10.1016/j.poly.2020.114488>.
- [19] M. Tafili-Kryeziu, M. Weil, T. Muranaka, A. Bousseksou, M. Hasegawa, A. Jun, W. Linert, Effect of the counter-anion on the spin-transition properties of a family of Fe(II) tetrazole complexes, [Fe(4tz)₆]X₂ (X = ClO₄⁻, PF₆⁻, SbF₆⁻, BF₄⁻), *Dalton Trans.* 42 (2013) 15796–15804, <https://doi.org/10.1039/C3DT52339J>.
- [20] G.-B. Yi, M.A. Khan, G.B. Richter-Addo, The first metalloporphyrin nitrosamine complex: bis(diethylnitrosamine)(meso-tetraphenylporphyrinato)iron(III) perchlorate, *J. Am. Chem. Soc.* 117 (1995) 7850–7851, <https://doi.org/10.1021/ja00134a048>.
- [21] L. Chen, G.-B. Yi, L.-S. Wang, U.R. Dharmawardana, A.C. Dart, M.A. Khan, G. B. Richter-Addo, Synthesis, characterization, and molecular structures of diethylnitrosamine metalloporphyrin complexes of iron, ruthenium, and osmium, *Inorg. Chem.* 37 (1998) 4677–4688, <https://doi.org/10.1021/ic9801591>.
- [22] N. Xu, L.E. Goodrich, N. Lehnert, D.R. Powell, G.B. Richter-Addo, Five- and six-coordinate adducts of nitrosamines with ferric porphyrins: structural models for the type II interactions of nitrosamines with ferric cytochrome P450, *Inorg. Chem.* 49 (2010) 4405–4419, <https://doi.org/10.1021/ic901751z>.
- [23] V.K.K. Praneeth, F. Paulat, T.C. Berto, S.D. George, C. Näther, C.D. Sulok, N. Lehnert, Electronic structure of six-coordinate iron(III)–Porphyrin NO adducts: the elusive iron(III)–NO(radical) state and its influence on the properties of these complexes, *J. Am. Chem. Soc.* 130 (2008) 15288–15303, <https://doi.org/10.1021/ja801860u>.
- [24] M. Trampuž, M. Znidarič, F. Gallou, Z. Časar, Does the red shift in UV–vis spectra really provide a sensing option for detection of N-nitrosamines using metalloporphyrins? *ACS Omega* 8 (2023) 1154–1167, <https://doi.org/10.1021/acsomega.2c06615>.
- [25] *CrysAlisPro (Version 1.171.39.46e)*, Rigaku Oxford Diffraction, Yarnton, UK, 2018.
- [26] G.M. Sheldrick, Shelxt – integrated space-group and crystal-structure determination, *Acta Crystallogr. A* 71 (2015) 3–8, <https://doi.org/10.1107/S2053273314026370>.
- [27] G.M. Sheldrick, Crystal structure refinement with SHELXL, *Acta Crystallogr. C* 71 (2015) 3–8, <https://doi.org/10.1107/S2053229614024218>.
- [28] O.V. Dolomanov, L.J. Bourhis, R.J. Gildea, J.A.K. Howard, H. Puschmann, OLEX2: a complete structure solution, refinement and analysis program, *J. Appl. Crystallogr.* 42 (2009) 339–341, <https://doi.org/10.1107/S0021889808042726>.
- [29] T. Knaflič, et al., Impact of Counter-anions on Structural and Magnetic Properties of iron(III) Meso-Tetraphenylporphyrin Tetrahydrofuran Solvates - Supplementary Information.
- [30] M. Nishi, Y. Hayata, N. Hoshino, N. Hanasaki, T. Akutagawa, M. Matsuda, Intermolecular interactions of tetraenzoporphyrin- and phthalocyanine-based charge-transfer complexes, *Dalton Trans.* 48 (2019) 17723–17728, <https://doi.org/10.1039/C9DT03653A>.
- [31] A. Malek, L. Latos-Grazynski, T.J. Bartczak, A. Zadlo, Reactions of the iron(III) tetraphenylporphyrin .pi. cation radical with triphenylphosphine and the nitrite anion. Formation of .beta.-substituted iron(III) porphyrins, *Inorg. Chem.* 30 (1991) 3222–3230, <https://doi.org/10.1021/ic00016a021>.
- [32] R. Patra, A. Chaudhary, S.K. Ghosh, S.P. Rath, Modulation of metal displacements in a saddle distorted macrocycle: synthesis, structure, and properties of high-spin

- Fe(III) porphyrins and implications for the hemoproteins, *Inorg. Chem.* 47 (2008) 8324–8335, <https://doi.org/10.1021/ic800944q>.
- [33] Z. Yao, C.E. Schulz, J. Yang, X. Li, J. Li, Intermolecular interactions and intramolecular couplings of binuclear porphyrin models for cytochrome c oxidase, *Inorg. Chem.* 59 (2020) 1242–1255, <https://doi.org/10.1021/acs.inorgchem.9b02958>.
- [34] S.C. Hunter, B.A. Smith, C.M. Hoffmann, X. Wang, Y.-S. Chen, G.J. McIntyre, Z.-L. Xue, Intermolecular interactions in solid-state metalloporphyrins and their impacts on crystal and molecular structures, *Inorg. Chem.* 53 (2014) 11552–11562, <https://doi.org/10.1021/ic5015835>.
- [35] M. Li, T.J. Neal, N. Ehlinger, C.E. Schulz, W.R. Scheidt, Inter-ring interactions in [Fe(TalkylP)(Cl)] (alkyl = ethyl, n-propyl, n-hexyl) complexes: control by meso-substituted groups, *J. Porphyr. Phthalocyanines* 14 (2010) 115–122, <https://doi.org/10.1142/S1088424610001714>.
- [36] T. Ikeue, Y. Ohgo, A. Uchida, M. Nakamura, H. Fujii, M. Yokoyama, High-spin (meso-Tetraalkylporphyrinato)iron(III) complexes as studied by X-ray crystallography, EPR, and dynamic NMR spectroscopies, *Inorg. Chem.* 38 (1999) 1276–1281, <https://doi.org/10.1021/ic981184+>.
- [37] S. Stoll, A. Schweiger, EasySpin, a comprehensive software package for spectral simulation and analysis in EPR, *J. Magn. Reson.* 178 (2006) 42–55, <https://doi.org/10.1016/j.jmr.2005.08.013>.
- [38] M. Sato, A.S. Rispin, H. Kon, EPR studies on high-spin Fe(III) tetraphenylporphine having rhombic character. Spin Hamiltonian and crystal field analysis of g values, *Chem. Phys.* 18 (1976) 211–224, [https://doi.org/10.1016/0301-0104\(76\)87048-6](https://doi.org/10.1016/0301-0104(76)87048-6).
- [39] J.R. Pilbrow, *Transition Ion Electron Paramagnetic Resonance*, Clarendon Press, 1990.